PNAS
www.pnas.org

Supplementary Information for

Current CaCO$_3$ dissolution at the seafloor caused by anthropogenic CO$_2$

Olivier Sulpis, Bernard P. Boudreau, Alfonso Mucci, Chris Jenkins, David S. Trossman, Brian K. Arbic, Robert M. Key

Olivier Sulpis
Email: olivier.sulpis@mail.mcgill.ca

This PDF file includes:

Supplementary text:
- Current speed sensitivity
- Anthropogenic CO$_2$ dataset
- Basis for equations 2 and 3 of the text and DBL control of dissolution
- Justification of the assumption of porewater saturation

Supplemental figures and Tables:
- Figs. S1 to S9
- Tables S1 to S2

References for citations in the SI

Supplementary Information Text
  Current speed sensitivity.

The bottom-ocean velocity field is generally poorly constrained. Significant qualitative and quantitative variations exist across various model output products, e.g., compare the dissipation rates that are proportional to bottom kinetic energy in Figs. 9b and 9c of Ref (1), and resolutions, e.g., compare Figs. 2a and 2c of Ref (2). To get a sense of the sensitivity of the beta parameter (β) and dissolution rates to different bottom speed products, we compared the results obtained from the bottom kinetic energy field of a $1/25^{th}$ degree global configuration of HYCOM, accounting for topographic internal lee-wave drag, with those obtained using a kinetic energy dataset from the same model without the "wave drag" effect, i.e., Fig. 3d and 3b of Ref. (3), respectively. Here, internal lee-wave drag represents the interaction between the bottom flows and the underlying topography that are not simply due to bottom friction. This drag is a momentum sink associated with internal lee-wave generation that arises from geostrophic flow impinging upon rough topography and topographic blocking. The results from this comparison are shown in SI Appendix, Fig. S7. Whereas the world-averaged bottom kinetic energy increases from 0.0066 m^2 s^{-2} using a model taking into account the wave-drag effect to 0.0171 m^2 s^{-2} for a model neglecting this effect (i.e., a 2.6 folds increase), the resulting carbonate ion mass-transfer coefficient (β) and calcite dissolution rate (r) are only moderately affected, as they rise from geometrically world-averaged values of $\beta = 14$ m yr^{-1} and $r = 0.10$ mol m^{-2} yr^{-1} to $\beta = 20$ m yr^{-1} and $r = 0.13$ mol m^{-2} yr^{-1}, respectively (a ~40 and 30% increase, respectively). Thus, our dissolution model, although impacted by the uncertainty in the current speed dataset, tends to attenuate these discrepancies. As shown in SI Appendix - Fig. S7, our results are not qualitatively affected by the initial bottom kinetic-model choice, as the loci of accelerated anthropogenically-driven dissolution are invariant whether or not the wave-drag effect is included in the initial kinetic energy model.

We chose two different bottom current-speed products because it is necessary to put an upper limit on the sensitivity of the dissolution rate changes over time. We focus on the relationship between bottom current-speed changes under a "climate change scenario" and the difference between the two bottom-current speed products used for this sensitivity analysis (i.e., with and without wave drag, see SI Appendix, Fig. S7). We posit that a comparison of their spatial patterns and magnitudes can inform us about the level of uncertainty in our dissolution rate change estimates. The focus here is on differences between each bottom current speed product because a bias that is consistent over time and space would approximately cancel out when considering its contribution to the changes in dissolution rates. The difference between the bottom current-speed products used here is larger than the simulated bottom current-speed change in climate change simulations over time (see Fig. 3e of Ref (4)) and at similar locations (namely, the Southern Ocean and the North Atlantic Ocean). This suggests that our estimates, based on the two bottom current speed products (with and without wave drag), can be used as an upper limit on the uncertainty of our dissolution rate change estimates.

Anthropogenic CO₂ dataset.

We have tested the sensitivity of our dissolution rates to the choice of the *DIC* dataset. Resolving or understanding the differences between various *DIC* datasets is beyond the scope of this paper, but we provide a comparison of the results described in the main text of this study, using the *DIC* dataset from Ref (5), with results obtained based on another *DIC* dataset from Ref (6). Both datasets comprise *DIC* values for the present day, as well as pre-industrial *DIC*, allowing us to compute and compare $\Delta[CO_3^{2-}]_{SW}$ and Δr. First, we note that $[CO_3^{2-}]_{SW}$ values computed with *DIC* from Ref (5), represented in Fig. 2a-b, are slightly lower than those derived with DIC from Ref (6), in SI Appendix, Fig. S8a-b. These differences are, however, not significant since they are within the error bars. $\Delta[CO_3^{2-}]_{SW}$ from Fig. 2c, using the DIC from Ref (5), reveals an anthropogenic $[CO_3^{2-}]_{SW}$ decrease of 4-8 μmol kg^{-1} in most of the bottom waters of the Atlantic and near the Southern Ocean, and the presence of a small anthropogenic signal in most of the bottom waters in the Pacific. On the other hand, $\Delta[CO_3^{2-}]_{SW}$ from SI Appendix - Fig. S8c, based on the alternative *DIC* dataset from Ref (6), shows an anthropogenic decrease in bottom $[CO_3^{2-}]_{SW}$ limited to shallow waters, along the Atlantic mid-ocean ridge and in the North Atlantic, while in most bottom waters, including those of the Indian and Pacific Oceans, no anthropogenic DIC seems to have been accumulated since the end of the pre-industrial era.

To examine in further detail the differences between these two datasets, we have plotted depth profiles showing the anthropogenic *DIC* concentration along the 170°W meridian, between 0 and 60°S, for both datasets, along with a depth profile showing the bottom-water CFC-11 concentration along the same section. CFC-11 is a non-reactive anthropogenic trace gas frequently used as an ocean tracer. CFC-11 emission to the atmosphere was virtually nonexistent before the end of World-War II, much later than that of anthropogenic CO₂ (~1950 vs ~1880). There are certainly differences in air-sea equilibration times and solubility, but in general, anywhere CFC-11 is found in bottom waters there should be anthropogenic *DIC* as well. As it can be seen in SI Appendix, Fig. S9, both *DIC* datasets show a northward progression of anthropogenic *DIC* in the bottom waters, but the magnitude of that increase varies. In both cases, the patterns of the anthropogenic *DIC* distribution fit those of the CFC-11, also showing a clear northward progression through the bottom waters. In addition, the dataset of Ref (6), that simulates anthropogenic *DIC* penetration from 1765 AD to 2011 AD, displays an anthropogenic *DIC* concentration of strictly zero for a large portion of the transect (between 2000 and 4000 m-depth, 40 and 0°S), whereas some CFC-11 is found in that area for the year 2009 AD. Anthropogenic *DIC* from Ref (5) is generally higher, and present in concentrations above zero in the entire depth profile, which is closer to the CFC-11 data. These observations support the assumption that the anthropogenic *DIC* dataset from Ref (5) is arguably more accurate than the dataset from Ref (6) for the purposes of the present study.

Comparing Fig. 3c with SI Appendix - Fig. S8f, it can be seen that the loci of anthropogenic dissolution are unaffected by the choice of the anthropogenic *DIC* dataset, with a major anthropogenic dissolution flux observed in the North Atlantic, and the presence of several dissolution hot spots in the most southern latitudes. Although Δr from Ref (6) is generally smaller than from Ref (5) and falls for the greater part within the error

bars, as shown in SI Appendix - Fig. S8f, some Δr values remain significant, such as the anthropogenic dissolution hotspots in the North and South Atlantic and in the Pacific. In addition, the CCD in the North West Atlantic rises from 5402 ± 346 m for the pre-industrial to 5086 ± 185 m for today when anthropogenic *DIC* from Ref (5) is used, compared to a rise to 5127 ± 183 m using Ref (6). These results are statistically identical. Thus, although the magnitudes of the dissolution rates are impacted by the initial choice of the DIC dataset, our results and conclusions are not. There is a clear indication for current anthropogenic dissolution of $CaCO_3$ at the seafloor and a shoaling of $CaCO_3$ marker horizons in the water column.

Basis for equation 2 and 3 of the text and DBL transport control of dissolution.

References (15-18) included the full complement of equilibrium and transport constraints of the CO_2-H_2O-system in a $CaCO_3$ diagenetic model. The effect of this inclusion was primarily to increase the rate of dissolution of $CaCO_3$ in sediments. Thus, a model that neglects the CO_2-system, as in earlier work by Refs (9) and (19), will under-estimate the amount of sedimentary $CaCO_3$ dissolution at a given ocean depth on the seafloor, an issue we will revisit below.

Reference (20) reconsidered the controls on $CaCO_3$ dissolution at the seafloor, including both the effects of a diffusive sublayer and reaction kinetics in the sediment. That paper based its analysis on the kinetic data in Ref. (21), which was the only study of $CaCO_3$ dissolution kinetics in natural sediments under seafloor-like conditions, at least until Ref. (22).

To establish the relative control of boundary layer effects versus sediment-side kinetics on $CaCO_3$ dissolution in a sediment, Ref. (20) created a hybrid diagenetic model for the carbonate ion alone in both the sediment and the boundary layer (see below). That paper does not include the full CO_2 system for the reason stated above, i.e., it would make the dissolution in the sediment faster and thus promote boundary layer control. With the Ref. (21) data, Ref. (20) could independently derive a mass transfer (rate) constant for dissolution in a bed of $CaCO_3$ and from boundary-layer theory, calculate the benthic boundary layer (BBL) mass-transfer coefficient. These results allowed Ref. (20) to determine which process (sediment-side kinetics versus BBL transport) controlled deep-sea $CaCO_3$ dissolution.

The Ref. (20) model is based on the following assumptions: steady state, infinitely fast mixing of the solid phase of the sediment, constant porosity of the sediment, constant dissolution parameters, and linear dissolution kinetics (justified below), while ignoring explicit treatment of the effects of oxic organic matter decomposition. While we know of no *data* that unambiguously demands a substantial role for organic matter oxidation in deep-sea $CaCO_3$ dissolution, we will nevertheless return to this point later.

4

Linear kinetics characterize the Ref. (21) data, as shown in a plot of rate (moles released to the overlying water per unit area and unit time) versus the degree of undersaturation, as reproduced below (Fig. A1).

A

B
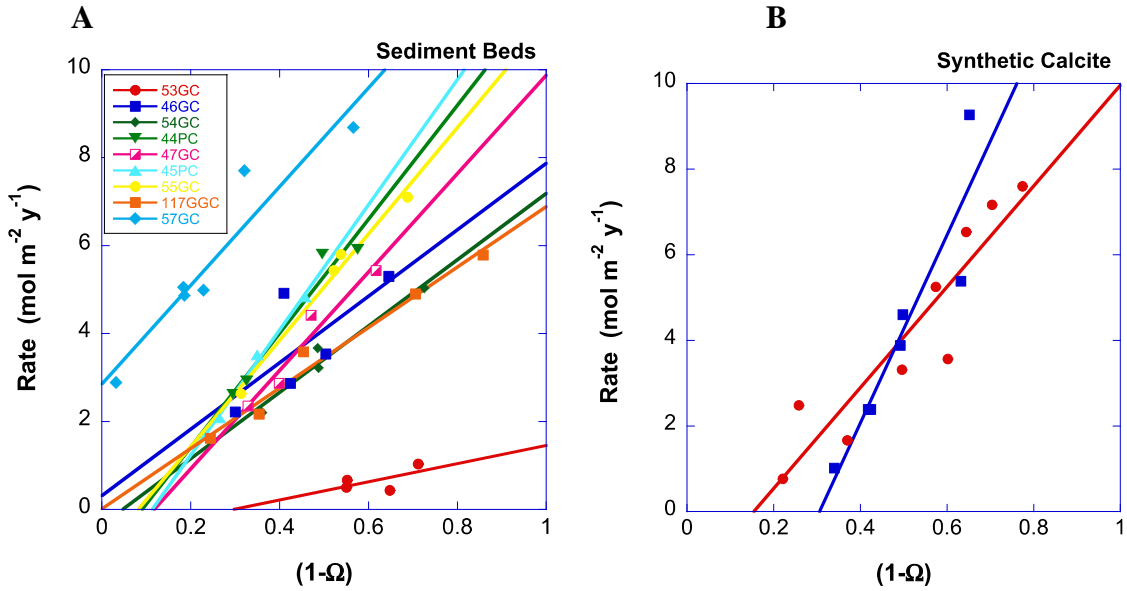
Figure A1. Calcite dissolution rates from Ref. (21), as re-plotted in Ref. (20), as a function of the reported degree of undersaturation.

These data are for real/natural deep-sea sediments (Fig. A1A) and beds of pure $CaCO_3$ (Fig. A1B); the rates for these two materials are very similar. Any argument that these data are anything but linear cannot be justified statistically. From these data, it is possible to extract a linear sediment-side rate constant (mass-transfer coefficient) for $CaCO_3$ dissolution in the bed as a function of the amount of $CaCO_3$ in the sediment (Fig. A2).
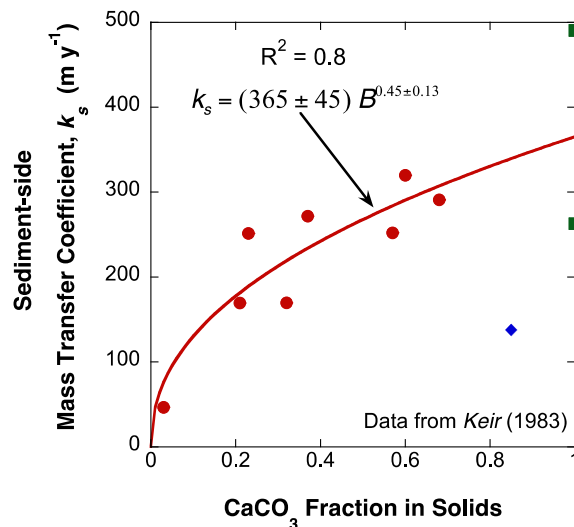
Figure A2. Calculated k_s values from the Ref. (21) data as re-analyzed in Ref. (20).

k_s in Fig. A2 is the sediment-side rate constant for the kinetic processes within the sediment (combined dissolution and diffusion) that Ref. (20) used to characterize $CaCO_3$ dissolution in that model, and we derive its specific mathematical form below.

Building upon linear dissolution kinetics (21-23), Ref. (20) used the following equations to describe the vertical distribution of dissolved and solid carbonate in sediments, as well as the "Clay" (non-carbonate) component of the solids.

   a)   For dissolved CO_3^{2-}

$$\varphi D_c \frac{d^2C}{dx^2} + (1-\varphi)k_c(C_s - C)B = 0$$

[A1]

where

    x is the depth into the sediment, with the origin at the sediment-water interface and a positive sign convention downward into the sediment.

    C is the carbonate ion concentration in the porewater

    C_s is the carbonate ion concentration in the porewater at saturation with $CaCO_3$

    D_c is the diffusion coefficient for carbonate ion in porewater, tortuosity corrected

    φ is the porosity of the sediment

    B is the *weight fraction* of the solids that is $CaCO_3$

    k_c is the pseudo-homogeneous rate constant for $CaCO_3$ dissolution in sediment (units of inverse time). It is not k_s, but instead the product of the real heterogeneous rate constant for dissolution per unit area of solid $CaCO_3$ surface multiplied by the total $CaCO_3$ surface area per unit volume of solid sediment

The first term in Eq. A1 accounts for diffusion in the porewaters, while the second term represents the source of dissolved carbonate from $CaCO_3$ dissolution into the porewaters.

b) For Calcite

$$F_B - \varphi D_c \frac{dC}{dx} = (1-\varphi)w\rho_{CaCO3}B$$

[A2]

where

    F_B is the flux (rain) of $CaCO_3$ to the seafloor

    w is the accumulation speed of the sediment

    ρ_{CaCO3} is the density of $CaCO_3$ (in units compatible to those of C)

c) For "Clay" (non-carbonate fraction of the solids)

$$F_M = (1-\varphi)\ w\ M$$

[A3]

where M is the mass concentration of "Clay" in the solids (kg m^{-3}) and F_M is the prescribed flux of "Clay" to the sediment-water interface (kg m^{-2} y^{-1}).

d) For Solid Volume Fraction

$$B + \frac{M}{\rho_m} = 1$$

[A4]

where ρ_M is the mass density of the "Clay" (kg m^{-3}).

Boundary conditions on this system of equations are:

$$-\varphi D_c \frac{dC}{dx}\bigg|_{x=0} = \beta(C_s - C_o)$$

(A5)

where C_0 is the dissolved carbonate ion concentration at the sediment-water interface and β is the effective mass-transfer coefficient on the water side of the sediment, i.e., the boundary layer. At depth in the sediment,

$$-\varphi D_c \frac{dC}{dx}\bigg|_{x\to\infty} = 0$$

[A6]

The solution to Eq. A1 is

$$C(x) = a_1 e^{-\sqrt{\kappa}x} + a_2 e^{+\sqrt{\kappa}x}$$

[A7]

where a_1 and a_2 are integration constants and

$$\kappa = \frac{(1-\varphi)k_c B}{\varphi D_c}$$

[A8]

Equation A6 then immediately gives that

$$a_2 = 0$$

[A9]

Equation A5 then gives that

$$a_1 = \frac{\beta(C_\infty - C_0)}{\varphi D_c \sqrt{\kappa}}$$

[A10]

The distribution of the solute in the diffusive boundary layer is linear,

$$C(x) = a_3 x + a_4$$

[A11]

7

where a_3 and a_4 are further constants.

The conditions on a_3 and a_4 are that $C(0) = a_4$ and $C(-\delta) = C_\infty$, where $x = -\delta$ is the top of the (diffusive) boundary layer. The second condition gives

$$a_3 = -\frac{(C_\infty - C_0)}{\delta}$$
[A12]

By matching Eqs. A7 and A11 at $x = 0$, there results an equation for the unknown concentration at the sediment-water interface,

$$C_0 = \frac{C_S + \dfrac{\beta C_\infty}{\varphi D_c \sqrt{\kappa}}}{1 + \dfrac{\beta}{\varphi D_c \sqrt{\kappa}}}$$
[A13]

B, the amount of $CaCO_3$ in the sediment, is obtained from Eq. A2; specifically, with Eq. A14,

$$F_B - k^* (C_\infty - C_s) = (1 - \varphi) w \rho_{CaCO3} B$$
[A14]

where (24,25)

$$k^* = \frac{k_s \beta}{k_s + \beta}$$
[A15]

and, k_s is then defined as,

$$k_s = \left[\varphi(1-\varphi) k_c D_c B \right]^{1/2}$$
[A16]

The burial speed w is obtained by combining and manipulating Eqs. A3, A4 and A14,

$$w = \frac{\left[F_B - k^* (C_\infty - C_s) \right]}{(1 - \varphi) \rho_{CaCO3}} + \frac{F_M}{(1 - \varphi) \rho_M}$$
[A17]

Equation A14 can be solved (numerically) to predict a $CaCO_3$ profile with ocean depth. When coupled with Equation A15, it also reveals that if $k_s \ll \beta$, the gradient in carbonate ion is in the porewaters and dissolution and diffusion within the sediment control the rate, whereas, if $k_s \gg \beta$ the rate is controlled by boundary layer transfer and the porewaters are essentially saturated.

We are now in a position to show that the $CaCO_3$-depth profiles in the oceans can be reproduced with this model. That can be done with Eqs A14-A17, if we supply values for the constants, where we focus on k_s and β. k_s is given in Fig A2 above, which is the experimentally-derived rate constants. β can be calculated as given in the *Methods* (also Ref. 27). Note that the $CaCO_3$ dissolution papers from the 1990s largely used k_c, and thus the implied k_s, as an adjustable parameter; for example, Refs (28 -36) all do this. These authors did this to explain observed pH profiles, which could not be accounted for with laboratory determined k_s or k_c values from sources other than Ref. (21). In other words, they lowered the value of k_c until they got a reasonable fit of the pH. That strategy is entirely based on circular logic and is thus self-fulfilling.

We can, however, assume that $k_s << \beta$ or $k_s >> \beta$ or use k* from Eq. A15 and thus show what a $CaCO_3$ depth profile would look like under sediment-side control, mass transfer control in the boundary layer or an intermediate scenario given by Eq. A15. Figs. A3A and A3B below show examples of these predicted $CaCO_3$ depth profiles for the North Eastern Atlantic and the Equatorial Pacific.

From Fig. A3 results, we can see that:

(1) *The case of k* = k_s, i.e., sediment-side kinetic control*. Using the unaltered laboratory determined rate constant k_s from Ref. (21), we do not reproduce most of the data in the NE Atlantic or any of the data in the Equatorial Pacific. Note that the same is true no matter what general area of the oceans you choose.

(2) *The case of k* = β, i.e., boundary-layer mass-transfer control*. Using the calculated effective mass-transfer coefficient for the boundary layer, the predictions match the data admirably, except for the tail, at very low $CaCO_3$ content. The same is true no matter what area of the oceans you choose.

(3) *Finally, using the exact k* from Eq. A15*. The green line captures the data trends including the tail. The same is true no matter what area of the oceans you choose. Note, however, that the $k* = \beta$ prediction agrees with this more precise prediction within the error in the data, except at the tail. Ref. (20) has further shown that the amount of $CaCO_3$ preserved in the tail is of not consequence to a $CaCO_3$ budget. The tail in this case is caused by the lack of enough $CaCO_3$ in the sediment to saturate the porewaters.

Figures A3A and A3B show that seabed $CaCO_3$ dissolution is largely controlled by mass transfer across the boundary layer. Inclusion of the full dissolved CO_2 system, i.e., adding equilibrium and transport of bicarbonate ion and aqueous CO_2, would increase the dissolution rate and raise all the predicted profiles to slightly higher depths. That makes the kinetic-controlled case an even worse predictor of the actual profiles.

Some investigators, in the past, have argued that the laboratory rates are somehow flawed and are much lower in situ. There is no evidence to support this contention; these opinions appear to be simply statements of belief. Keir's experiments were carried out with seawater and natural sediments. To invoke an identified retarding/inhibition effect that

occurs in the ocean but not the laboratory is baseless. (Yes, there were no macrofauna in the lab case, but digestion of $CaCO_3$ hurries its dissolution.)

Can Keir's rate be reproduced to establish their validity? Reference (22) redid the Keir experiments, but with better stirring control. Keir's results did not indicate any real difference between natural and synthetic calcite. Reference (22) found that the rate of dissolution of a $CaCO_3$ bed was:

(1) a *linear* function of the degree of undersaturation, just as in Fig. A1 of the Ref. (21) data, as shown by Fig. A4 below,

(2) had *similar dependence* of the rate on the $CaCO_3$ content of the bed (Fig. A2), as shown by Fig. A5 below. Note, the *interface area-normalized* sediment-side rate constant (yet another form of rate constant!) derived in Ref. (22) (14.3 ± 1.5 mol m^{-2} yr^{-1}) is only slightly higher to that obtained from a fit to Ref. (21) calcite dissolution experimental results (10.5 ± 1.5 mol m^{-2} yr^{-1}).

(3) finally, the rate of dissolution is demonstrably dependent on the stirring rate of the overlying water at lower stirring speeds, as shown by Fig. A6 below, which is not possible with sediment-side kinetic control. The higher stirring rates are far beyond any mixing that could occur in the oceans.

The results summarized above constitute our evidence for a (largely) water-side mass-transfer control on deep-sea $CaCO_3$ dissolution on the ocean floor.
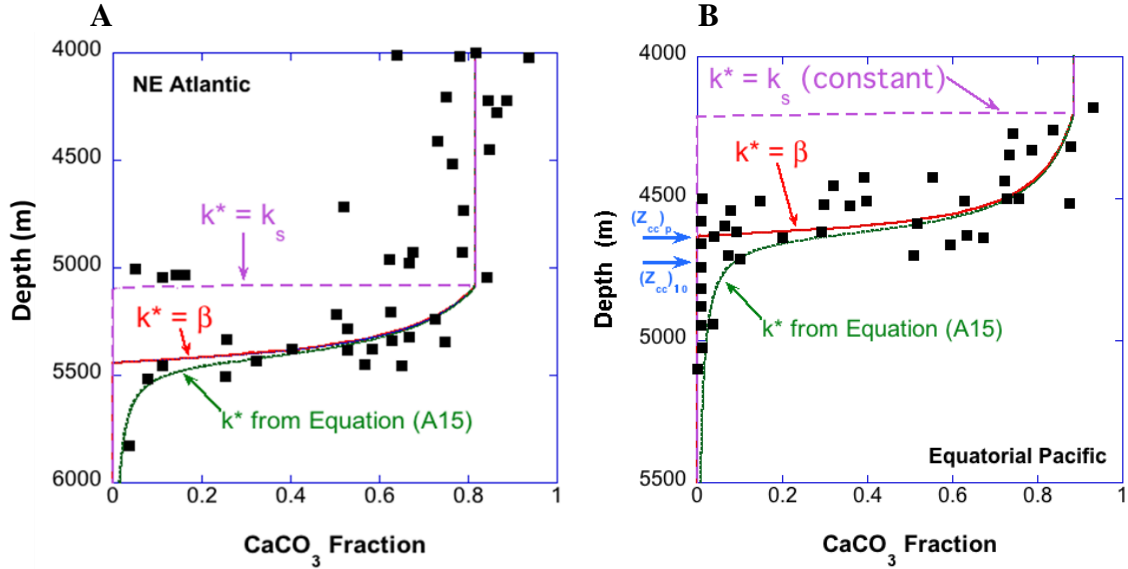
Figure A3. Predicted CaCO₃ distribution profiles with Eq. A14, as modified from Ref. (20). Note $(Z_{cc})_p$ in the right-hand diagram indicates the depth of the (potential) CCD if dissolution is completely controlled by DBL mass transfer (27), while $(Z_{cc})_{10}$ indicates the standard estimated depth for the CCD assuming it corresponds to the depth where the CaCO₃ content of the sediment falls to 10%.
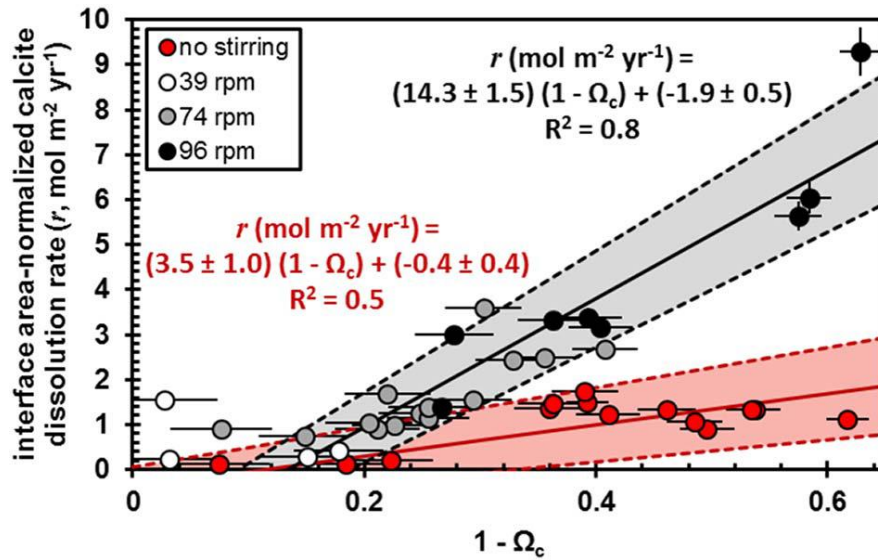
Figure A4. Steady-state ISA-normalized calcite dissolution rate as a function of the steady-state undersaturation state $(1 - \Omega_c)$. The color of each point represents the stirring speed used during the dissolution experiments. Uncertainties are represented by error bars on both the saturation state and the dissolution rate. The red and the black solid lines are, respectively, the linear bivariate fit to the experimental dissolution data obtained in unstirred, i.e., Eq. 7a in Ref. (22), and stirred reactors, Eq. 8b in Ref. (22), and the dashed lines describe the standard errors for each model. Taken from Ref. (22).
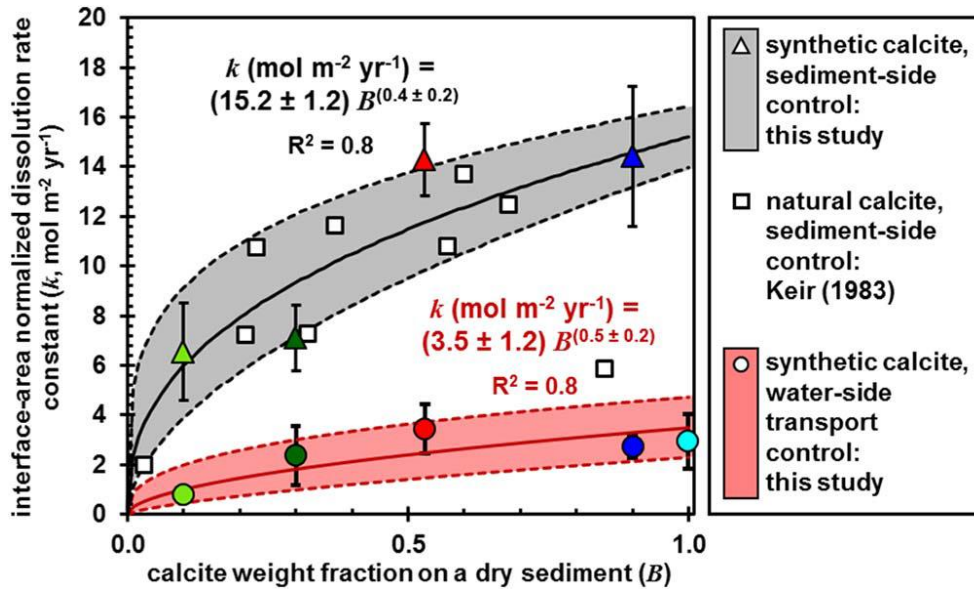
Figure A5. The apparent ISA-normalized rate constants (k, with error bars) as a function of the calcite content (B) of the sediment disks. The circles are rate constants from experiments carried out under quiescent conditions and the triangles are rate constants from experiments in stirred (74 rpm) reactors. The solid lines are standard power regression models and their equations are displayed above each data group with uncertainties, represented by the dashed lines, on both the slope and the order of dependence on the calcite weight fraction. The white squares are dissolution rate constants derived from experiments carried out by Ref. (21) on natural deep-sea calcitic sediments. Taken from Ref. (22).
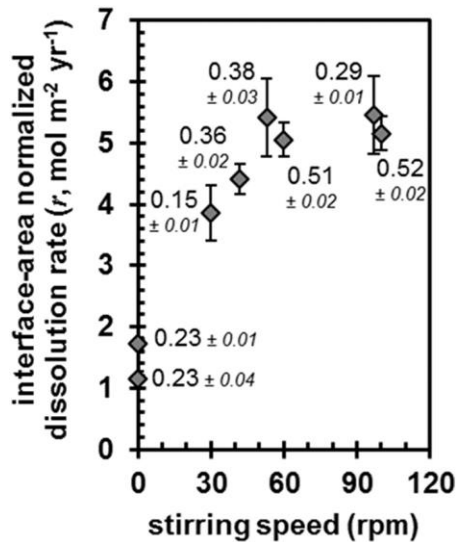
Figure A6. Indiana limestone calcite dissolution rates as a function of the stirring speed. The labels indicate the measured steady-state saturation state with respect to calcite ($\Omega_{calcite}$) in the bulk seawater for each experiment. Taken from Ref. (22).

Justification of the assumption of porewater saturation.

The importance of the DBL limitation on the $CaCO_3$ dissolution at the seafloor has been emphasized by several research groups in the past (9, 19-22, 37). As explained in Ref. (24), if the DBL resistance on the dissolution flux of calcite from a sediment is much greater than the internal resistance, i.e., the sum of the kinetic and diffusional resistance within the porewaters, the overall reaction rate is controlled by mass transfer through the DBL. This is the case when $k_S \gg \beta$. Under this "external diffusion regime", the concentration at the interface must be near $[CO_3^{2-}]_{eq}$. This scenario corresponds to Fig. 6-5c in Ref. (24). Because the mass transfer coefficient β is primarily a function of the flow characteristics, the reaction rate is determined by the hydrodynamics and not by kinetics of reactions occurring at the interface or within the sediments. Thus, the $CaCO_3$ dissolution rate at the seafloor should be controlled by diffusion through the DBL if $[CO_3^{2-}]_{sw}$ in the porewaters is equal or close to $[CO_3^{2-}]_{eq}$, a situation that can be achieved if the dissolution kinetics of the individual $CaCO_3$ grains within the sediment are fast.

The calcite dissolution rates derived from laboratory experiments where calcite grains are kept in suspension in a reactor, e.g., Refs (38-41), thus free of any diffusion limitation, are consistently orders of magnitude higher than the dissolution rates from experiments performed on sediments subject to the presence of a DBL, e.g., Refs (20-22), when the considered dissolving surface area is the same. As noted in Ref. (24), because a typical 1 mm-thick DBL is ~100 thicker than the boundary layer around 10 μm particles, and because the specific surface area of natural calcitic particles is very large, the internal resistance of deep-sea sediments is significantly lower than their external resistance, due to the presence of a DBL above the interface. Thus, diffusion through the DBL is by far the slowest step in the kinetics of calcite dissolution at the seafloor, and $[CO_3^{2-}]_{sw}$ should tend towards $[CO_3^{2-}]_{eq}$ at the interface, as the porewaters would be saturated with respect to calcite.

Although Ref. (28) reported calcite dissolution within the first cm of deep-sea sediments, this dissolution may be due to metabolic processes, or experimental bias caused by the introduction of microelectrodes through the sediment-water interface. Ref. (42) showed that early micro-electrodes, inserted into sediments from the water-side of the SWI, measured deeper O_2 penetration in sediments than electrodes inserted from below and moved upward. The microelectrodes inserted from the water-side caused overlying water to penetrate the sediment to some extent; if this afflicted the Ref. (28) study, then undersaturated overlying waters may have been introduced into the sediment, leading to dissolution at depths where no dissolution was occurring previous to electrode insertion. Besides, we also note that Ref. (28) did not measure calcite dissolution directly but, instead, computed this dissolution based on porewater chemistry, assuming a reaction order of 4.5 (following the results of Ref. (39) obtained under very different hydrodynamic conditions, i.e., particles in suspension) and fitting a dissolution rate constant to these data. Thus, we do not believe that the study of Ref. (28) provides any evidence invalidating the concept of calcite dissolution in sediments occurring primarily at the SWI. In fact, compelling evidence has been brought following the publication of Ref. (28) to support the theory of external diffusion regime for calcite dissolution at the seafloor. Several studies concluded

that calcite dissolution must primarily take place *at* or *just below* the sediment-water interface (before the grains get buried) rather than in the underlying mixed zone, in order to explain the observed distribution calcite radiocarbon ages in sediment profiles, e.g., Refs. (43-45). Similarly, Ref. (22) measured no discernable depth-gradient in the calcite content of synthetic calcite-rich sediment disks undergoing dissolution at the end of the dissolution experiments.

Consequently, abundant theory and data support the strong dependency between bottom-current speed and the calcite dissolution rate at the SWI that is being supported in our study, suggesting that for most of the calcitic sediments at the seafloor, porewater $[CO_3^{2-}]$ near the sediment-water interface is equal or close to $[CO_3^{2-}]_{eq}$, and that the dissolution reaction of calcite at the seafloor is mostly water-side transport controlled.

Supplementary figures and tables
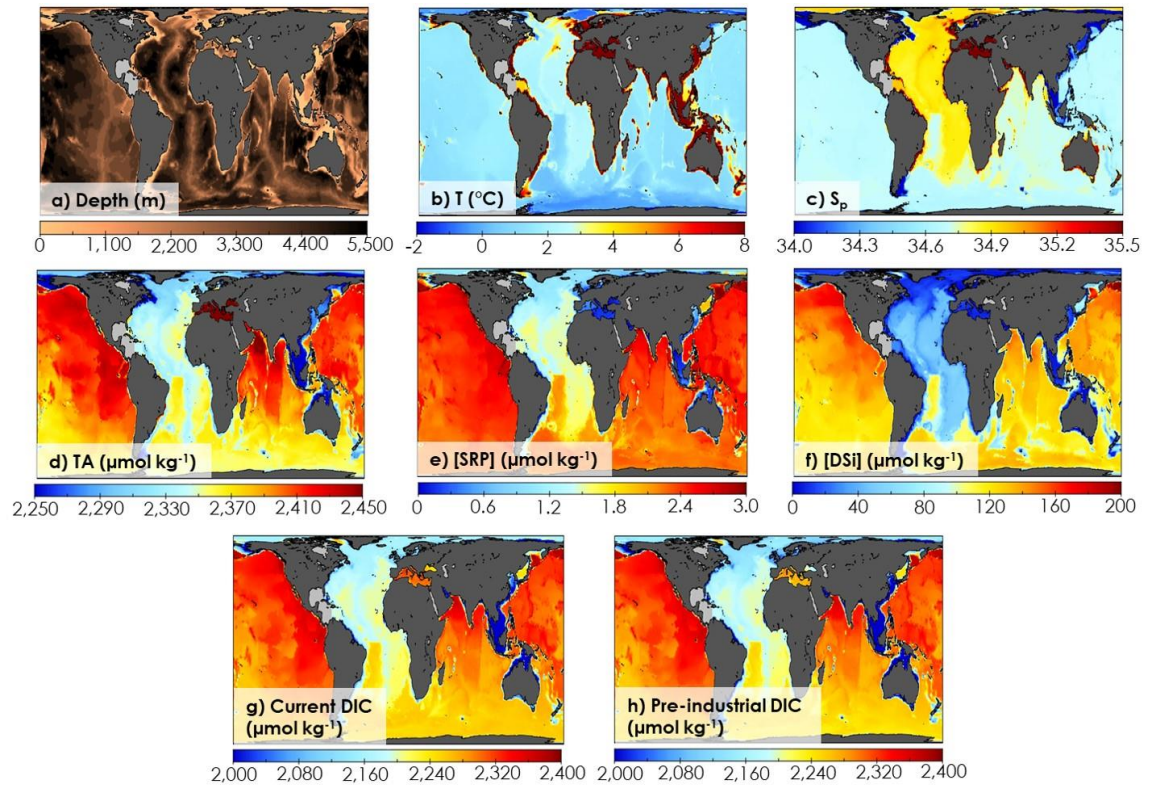
Fig. S1. Bottom-water distribution of the GLODAPv2.2016b variables used in the computation of $[CO_3^{2-}]_{SW}$. (**a**) depth of the deepest resolved layer of GLODAPv2.2016b considered to be bottom waters, (**b**) temperature (T), (**c**) practical salinity (S_p) , (**d**) total alkalinity (TA), (**e**) soluble reactive phosphate (SRP) concentration, (**f**) dissolved inorganic silica (DSi) concentration, (**g**) current and (**h**) pre-industrial dissolved inorganic carbon (DIC) concentrations.
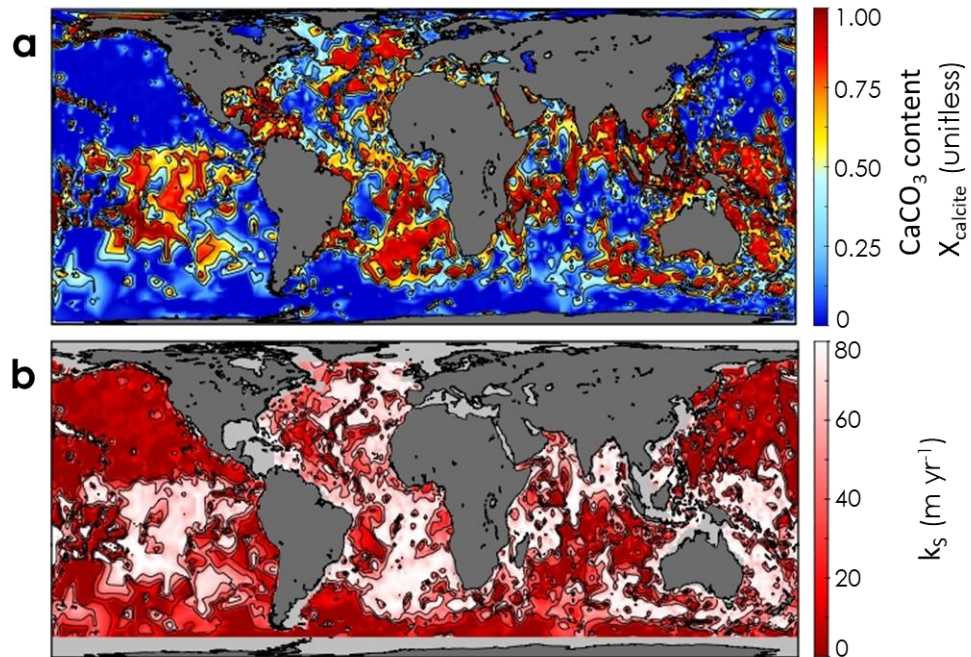
Fig. S2. **(a)** Global-scale CaCO$_3$ content of surficial sediments and **(b)** sediment-side CO$_3^{3-}$ mass-transfer coefficient computed using Eq. 10.
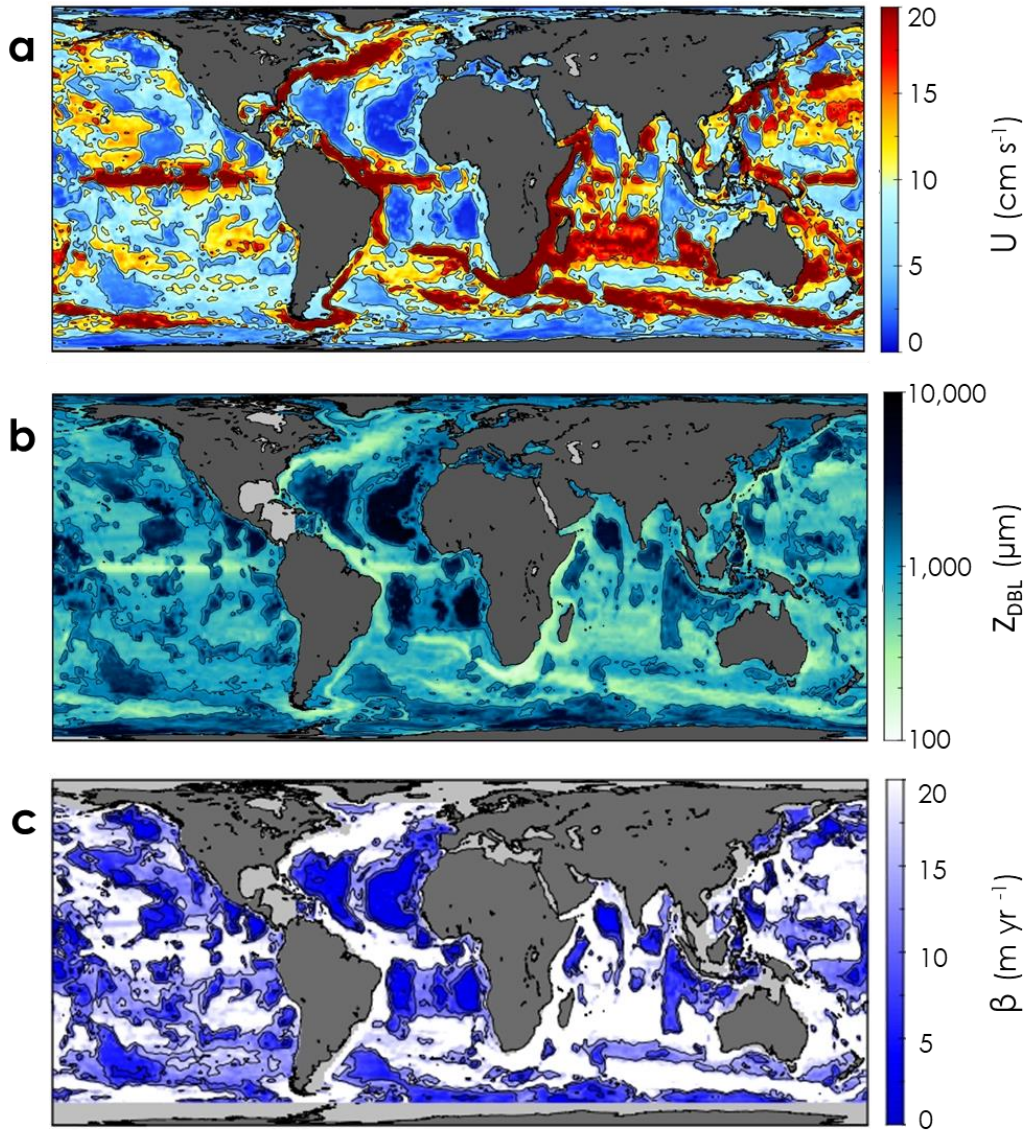
Fig. S3. Diffusive boundary layer thickness as a function of the bottom-current velocity. (**a**) Current speed resolved by the 1/25th degree HYCOM simulation, averaged over the final year of its run and over the bottom 500 meters, (**b**) diffusive boundary layer thicknesses at the sediment-water interface and (**c**) water-side CO_3^{2-} mass-transfer coefficient.
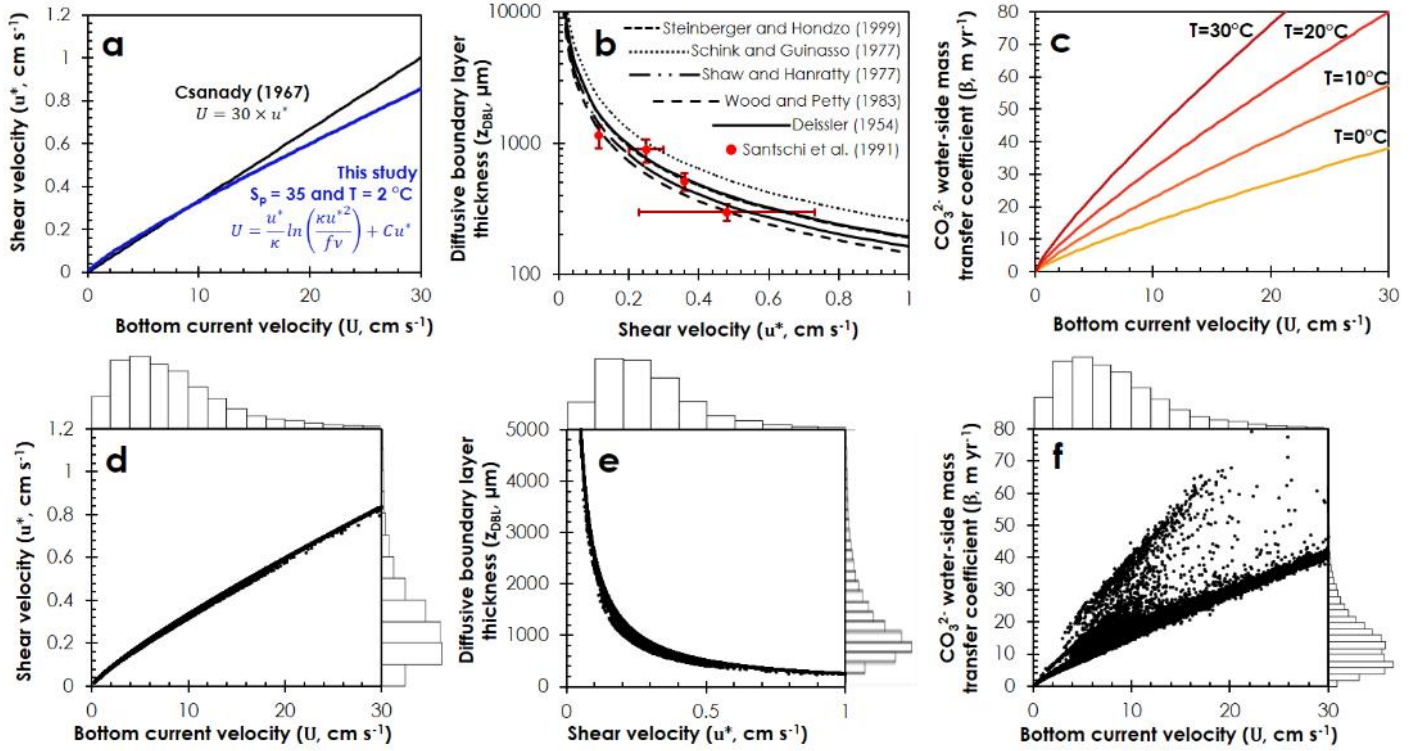
Fig. S4. Impact of temperature and current velocity on the water-side CO_3^{2-} mass-transfer coefficient and the DBL thickness. (**a**) Shear velocity ($u*$) as a function of the current velocity (U) at the outer edge of the bottom boundary layer, according to the equation derived in this study (in blue) and to the empirical equation from Csanady in ref. (8). (**b**) DBL thickness (z_{DBL}) as a function of the shear velocity($u*$) for 5 different empirical models (9-13) and comparison with observation-based DBL thicknesses from Santschi et al. in Ref. (14). (**c**) Water-side CO_3^{2-} mass-transfer coefficient (β) as a function of the current velocity (U) at various temperatures. (**d-f**) Plots representing the entirety of the data on the seafloor, where each black point represents one 1°x1° value. Each plot is associated with a histogram on each of its axes showing the relative distribution of the data over the range observed at the seafloor.
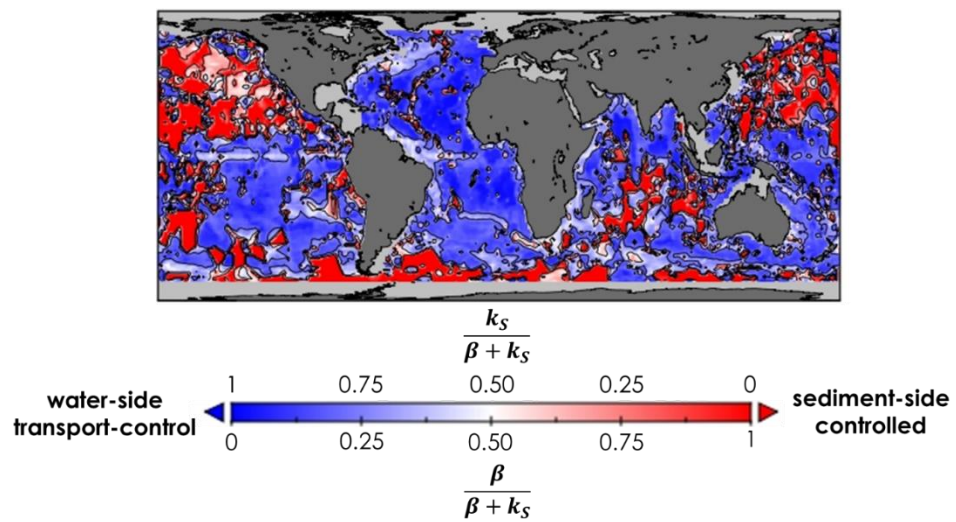
Fig. S5. Relative control from the sediment-side (k_S) or water-side (β) mass-transfer coefficients on the overall CO_3^{2-} mass transfer coefficient (k^*).
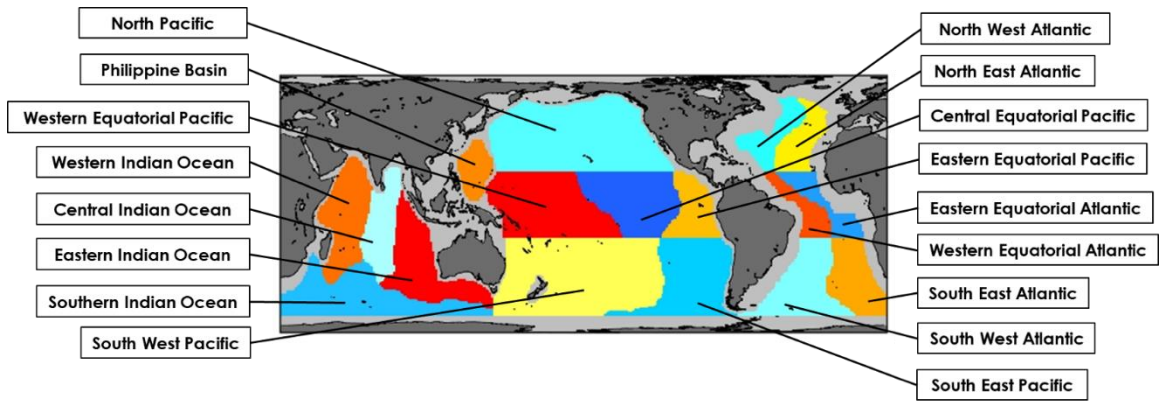
**Fig. S6.** Geographical boundaries of the 11 regions used to estimate the CCD from the calcite contents of sediments ($X_{calcite}$). The Southern Ocean, the Arctic Ocean, and all depths shallower than 300 m are not included in our CCD estimates.
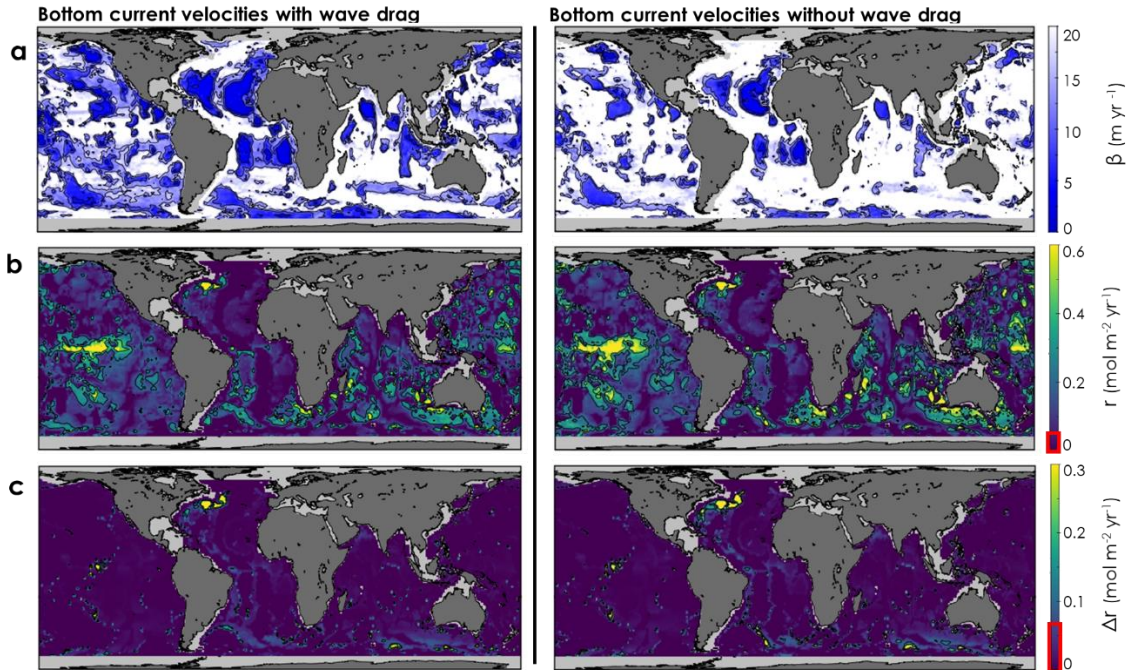
Fig. S7. Sensitivity of the dissolution rate model to two different initial kinetic energy distribution models. Impact of the "wave drag" effect on (**a**) the water-side CO_3^{2-} mass-transfer coefficient (β), (**b**) the current calcite dissolution rates at the sediment-water interface (r), and (**c**) the difference between pre-industrial and current calcite dissolution rates below 300 m (Δr = current r – pre-industrial r). Uncertainties are indicated by the red outline on the color bars, corresponding to one standard deviation, equal to 0.05 mol m yr^{-1} for r and to 0.07 mol m yr^{-1} for Δr.
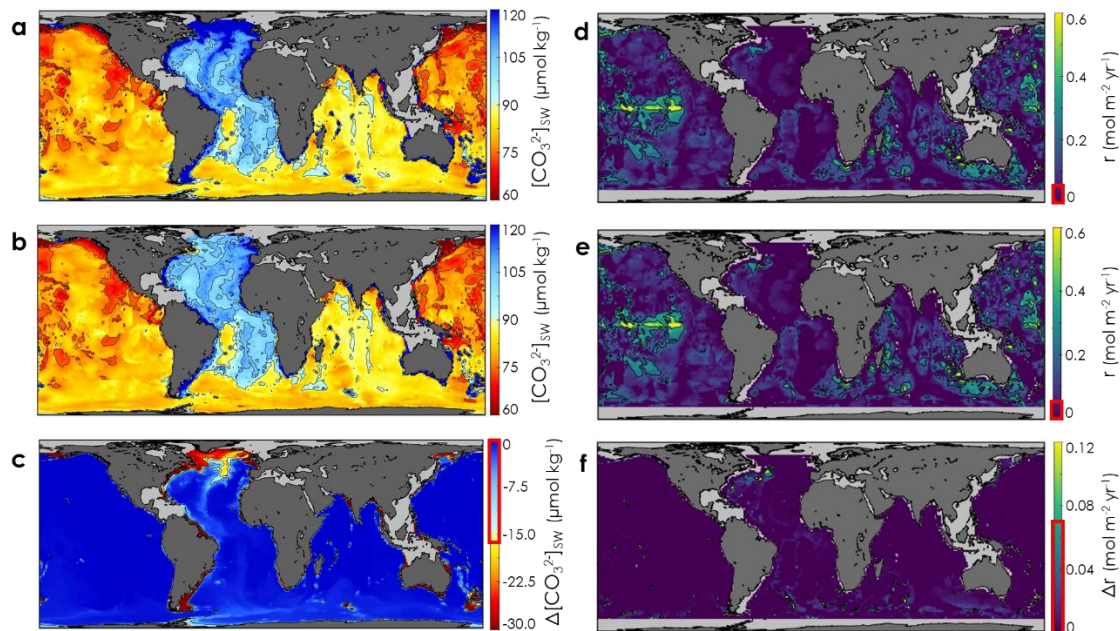
Fig. S8. Bottom-water $[CO_3^{2-}]$ and calcite dissolution rates estimated from an alternate DIC dataset from ref. (6). The panels on the left depict (**a**) pre-industrial bottom-water $[CO_3^{2-}]_{SW}$, (**b**) current bottom-water $[CO_3^{2-}]_{SW}$ and (**c**) difference between pre-industrial and current bottom-water $[CO_3^{2-}]_{SW}$ ($\Delta[CO_3^{2-}]_{SW}$ = current bottom-water $[CO_3^{2-}]_{SW}$ minus pre-industrial bottom-water $[CO_3^{2-}]_{SW}$), below 300 m. The panels on the right represent (**d**) pre-industrial, (**e**) current calcite dissolution rates (r) at the sediment-water interface, and (**f**) the difference between pre-industrial and current calcite dissolution rates below 300 m (Δr = current r minus pre-industrial r), i.e., the anthropogenic CO_2-driven calcite dissolution rate. Uncertainties are indicated by the red outline on the color bars, corresponding to one standard deviation, equal to 16.9 µmol kg^{-1} for $\Delta[CO_3^{2-}]_{SW}$, to 0.05 mol m yr^{-1} for r and to 0.07 mol m yr^{-1} for Δr.
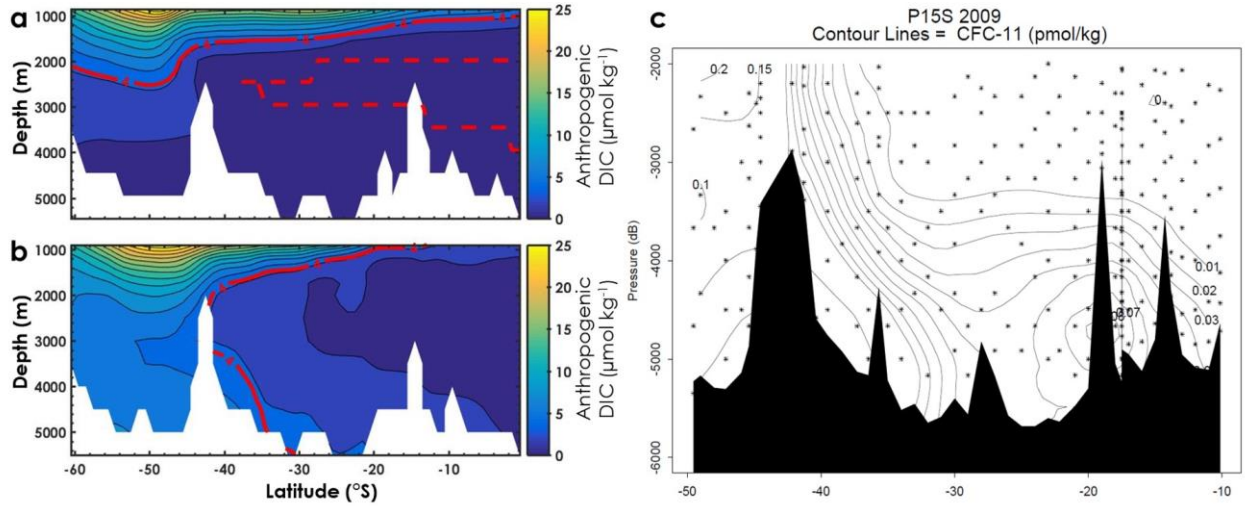
Fig. S9. Anthropogenic tracers penetration in the ocean bottom waters. Concentration profiles along the 170°W meridian, in the southern hemisphere and below 1000m, of (**a**) anthropogenic DIC from ref (6), (**b**) anthropogenic DIC from refs (5,7) and (**c**) CFC-11 (note that 2 different contour intervals are used, 0.05 and 0.01 for low concentration areas). The solid red lines in the left panels represent the anthropogenic DIC detection limit that we set to 4 µmol kg⁻¹, below which an anthropogenic DIC addition would not be considered significant, and the red dashed lines delimit the areas where no anthropogenic DIC is found, i.e., its estimated concentration is strictly zero.

Table S1. Regional averages of pre-industrial and current calcite marker horizons and dissolution rates.

	Pre-industrial values (ca. 1800 AD)				Current values (2002 AD)			
	CCD (m)	CSD (m)	r (mol m^{-2} yr^{-1})	global r (x10^{12} mol yr^{-1})	CCD (m)	CSD (m)	r (mol m^{-2} yr^{-1})	global r (x10^{12} mol yr^{-1})
North West Atlantic	5402 ± 346 (n=26)	4866 ± 180	0.02 ± 0.03	0.1 ± 0.2	5086 ± 185	4524 ± 206	0.05 ± 0.03	0.3 ± 0.2
North East Atlantic	5402 ± 441 (n=7)	4756 ± 174	0.02 ± 0.02	0.1 ± 0.1	5253 ± 178	4592 ± 203	0.02 ± 0.02	0.1 ± 0.1
Western Equatorial Atlantic	4896 ± 363 (n=5)	4187 ± 234	0.06 ± 0.03	0.3 ± 0.2	4767 ± 215	4040 ± 248	0.07 ± 0.03	0.3 ± 0.2
Eastern Equatorial Atlantic	5926 ± 155 (n=8)	4542 ± 205	0.03 ± 0.03	0.2 ± 0.2	5853 ± 161	4446 ± 212	0.03 ± 0.03	0.2 ± 0.2
South West Atlantic	4407 ± 569 (n=15)	3573 ± 299	0.05 ± 0.02	0.7 ± 0.3	4180 ± 280	3288 ± 334	0.07 ± 0.02	1.0 ± 0.3
South East Atlantic	4491 ± 475 (n=5)	3834 ± 269	0.08 ± 0.05	0.9 ± 0.6	4358 ± 251	3667 ± 287	0.10 ± 0.05	1.1 ± 0.6
North Pacific	4422 ± 990 (n=24)	2910 ± 388	0.09 ± 0.06	3.2 ± 2.2	4386 ± 293	2861 ± 395	0.09 ± 0.06	3.2 ± 2.2
Western Equatorial Pacific	4671 ± 400 (n=19)	3101 ± 360	0.14 ± 0.05	3.1 ± 1.0	4641 ± 269	3056 ± 366	0.14 ± 0.05	3.1 ± 1.0
Central Equatorial Pacific	4432 ± 386 (n=18)	3178 ± 349	0.19 ± 0.06	3.2 ± 1.0	4412 ± 276	3152 ± 353	0.20 ± 0.06	3.3 ± 1.0
Eastern Equatorial Pacific	3895 ± 377 (n=10)	2781 ± 408	0.09 ± 0.04	0.7 ± 0.3	3876 ± 331	2756 ± 412	0.09 ± 0.04	0.7 ± 0.3
South West Pacific	4320 ± 308 (n=32)	3232 ± 341	0.11 ± 0.06	4.2 ± 2.2	4239 ± 287	3105 ± 359	0.12 ± 0.06	4.6 ± 2.2
South East Pacific	4036 ± 195 (n=9)	3114 ± 359	0.08 ± 0.05	1.5 ± 0.9	3967 ± 308	3032 ± 370	0.09 ± 0.05	1.7 ± 0.9
Philippine Basin	4077 ± 312 (n=7)	2864 ± 395	0.10 ± 0.07	0.5 ± 0.3	4047 ± 316	2825 ± 401	0.10 ± 0.07	0.5 ± 0.3
Western Indian Ocean	4765 ± 300 (n=6)	3459 ± 312	0.12 ± 0.04	1.6 ± 0.5	4747 ± 245	3414 ± 318	0.13 ± 0.04	1.7 ± 0.5
Central Indian Ocean	4439 ± 674 (n=6)	3490 ± 309	0.10 ± 0.06	0.9 ± 0.6	4403 ± 261	3445 ± 315	0.11 ± 0.06	1.0 ± 0.6
Eastern Indian Ocean	5214 ± 346 (n=7)	3458 ± 313	0.16 ± 0.04	2.5 ± 0.7	5134 ± 231	3344 ± 328	0.19 ± 0.04	2.9 ± 0.7
Southern Indian Ocean	4346 ± 533 (n=8)	3473 ± 312	0.07 ± 0.05	1.4 ± 0.9	4130 ± 288	3212 ± 345	0.10 ± 0.05	2.0 ± 0.9

Pre-industrial CCD (calcite compensation depth) estimated from carbonate content of surficial sediments, current CCD, pre-industrial and current CSD (calcite saturation depth) computed from GLODAPv2.2016b data, regional averages of the calcite dissolution rate (mol m^{-2} yr^{-1}) and global rates (x10^{12} mol yr^{-1}). Also reported are the standard deviations associated with each horizon and the number (n) of data points from the dbSEABED database used to derive pre-industrial CCD from the calcite contents of the sediments.

Table S2. Equations used for the computation of standard deviations.

Variable	Standard deviation

F

$$\sigma_F = k^* \sqrt{\left(\frac{K_{sp}^*}{[Ca^{2+}]}\right)^2 e^{\frac{CCD\,\rho\,g}{p_c}} \left(\frac{\sigma_{CCD}\,\rho\,g}{p_c}\right) \sqrt{\left(\frac{\sigma K_{sp}^*}{K_{sp}^*}\right)^2 + \left(\frac{\sigma S_p}{S_p}\right)^2} + \sigma_{[CO_3{}^{2-}]_{SW}}{}^2}$$

r

a. $\quad \sigma_r = \sigma_F$

b. $\quad \sigma_r = k^* \sqrt{[CO_3{}^{2-}]_{eq}{}^2 \left(\left(\frac{\sigma K_{sp}^*}{K_{sp}^*}\right)^2 + \left(\frac{\sigma S_p}{S_p}\right)^2\right) + \sigma_{[CO_3{}^{2-}]_{SW}}{}^2}$

c. $\quad \sigma_r = \sqrt{\sigma_F{}^2 + (k^*)^2 \left([CO_3{}^{2-}]_{eq}{}^2 \left(\left(\frac{\sigma K_{sp}^*}{K_{sp}^*}\right)^2 + \left(\frac{\sigma S_p}{S_p}\right)^2\right) + \sigma_{[CO_3{}^{2-}]_{SW}}{}^2\right)}$

Δr

$$\sigma_{\Delta r} = \sqrt{\sigma_{current\,r}{}^2 + \sigma_{preindustrial\,r}{}^2}$$

[CO₃²⁻]ₛw

$$\sigma_{[CO_3{}^{2-}]_{SW}} = \sqrt{\sigma_{TA}{}^2 + \sigma_{DIC}{}^2}$$

Δ[CO₃²⁻]ₛw

$$\sigma_{\Delta[CO_3{}^{2-}]_{SW}} = \sqrt{\sigma_{current\,[CO_3{}^{2-}]_{SW}}{}^2 + \sigma_{preindustrial\,[CO_3{}^{2-}]_{SW}}{}^2}$$

This table reports the formulas used to compute the standard deviation associated with each computed variable. For *r*, the standard deviation was derived using either equations a, b or c reported in this table, depending on the equation used to define *r*, Eqs. 12, 13 and 14, respectively.

Supplementary references

1. Arbic BK, et al. (2009) Estimates of bottom flows and bottom boundary layer dissipation of the oceanic general circulation from global high-resolution models. *J Geophys Res* 114.
2. Thoppil PG, Richman JG, Hogan PJ (2011) Energetics of a global ocean circulation model compared to observations. *Geophys Res Lett* 38.
3. Trossman DS, et al. (2016) Impact of topographic internal lee wave drag on an eddying global ocean model. *Ocean Model* 97:109-128.
4. Melet A, Hallberg R, Adcroft A, Nikurashin M, Legg S (2015) Energy Flux into Internal Lee Waves: Sensitivity to Future Climate Changes Using Linear Theory and a Climate Model. *J Climate* 28:2365-2384.
5. Lauvset SK, et al. (2016) A new global interior ocean mapped climatology: the $1° \times 1°$ GLODAP version 2. *Earth Syst Sci Data* 8:325-340.
6. Khatiwala S, Primeau F, Hall T (2009). Reconstruction of the history of anthropogenic CO_2 concentrations in the ocean. *Nature* 462.
7. Key RM, et al. (2015) Global Ocean Data Analysis Project, Version 2 (GLODAPv2), ORNL/CDIAC-162, NDP-P093. Carbon Dioxide Information Analysis Center, Oak Ridge National Laboratory, US Department of Energy, Oak Ridge, Tennessee.
8. Csanady GT (1967) On the "Resistance Law" of a Turbulent Ekman Layer. *J Atmos Sci* 24:467-471.
9. Schink D, Guinasso N (1977) Modelling the influence of bioturbation and other processes on calcium carbonate dissolution at the sea floor. *The fate of fossil fuel CO_2 in the oceans*, eds Andersen NR, Malahoff A (Plenum Press), pp 375-400.
10. Steinberger N, Hondzo M (1999) Diffusional Mass Transfer at Sediment-Water Interface. *J Environ Eng* 125(2):192-200.
11. Deissler RG (1954) Analysis of turbulent heat transfer, mass transfer, and friction in smooth tubes at high Prandtl and Schmidt numbers. *National Advisory Commitee Aerodynamics, Technical Note 3145.* U.S. Government Printing Office, Washington D.C.
12. Shaw DA, Hanratty TJ (1977) Turbulent mass transfer rates to a wall for large Schmidt numbers. *AIChE J* 23(1):28-37.
13. Wood PE, Petty CA (1983) New model for turbulent mass transfer near a rigid interface. *AIChE J* 29(1):164-167.
14. Santschi PH, Anderson RF, Fleisher MQ, Bowles W (1991) Measurements of diffusive sublayer thicknesses in the ocean by alabaster dissolution, and their implications for the measurements of benthic fluxes. *J Geophys Res* 96(C6):10641-10657.
15. Boudreau BP (1987) A steady-state diagenetic model for dissolved carbonate species and pH in the porewaters of oxic and suboxic sediments. *Geochim. Cosmochim. Acta* 51: 1985-1996.
16. Boudreau BP (1996) A method-of-lines code for Carbon and nutrient diagenesis. *Comput. Geosci.* 22: 479-496.
17. Boudreau BP, Canfield DE (1988) A provisional diagenetic model for pH in anoxic porewaters: Application to the FOAM site. *J. Mar. Res.* 46: 429-455.
18. Boudreau BP, Canfield DE (1993) A comparison of closed and open-system models for porewater pH and calcite saturation. *Geochim. Cosmochim. Acta* 22: 317-334
19. Takahashi T., Broecker WS (1977) Mechanisms for calcite dissolution on the sea floor. *The Fate of Fossil Fuel CO_2 in the Oceans*, eds Andersen NR, Malahoff A (Plenum Press), pp 455-477.
20. Boudreau BP (2013) Carbonate dissolution rates at the deep ocean floor. *Geophys Res Lett* 40:744-748.

21   Keir RS (1983),Variation in the carbonate reactivity of deep-sea sediments: determination from flux experiments. *Deep Sea Res., Part A* 30: 279–296, doi:10.1016/0198-0149(83)90011-0.

22   Sulpis O, Lix C, Mucci A, Boudreau BP (2017) Calcite dissolution kinetics at the sediment-water interface in natural seawater. *Mar Chem* 195:70-83.

23   Hales, B, Emerson, SR (1997) Evidence in support of first-order dissolution kinetics for calcite in seawater. Eath Planet. Sci. Lett. 148, 317-327.

24   Boudreau, BP, Guinasso, NL (1982) The influence of a diffusive sublayer on accretion, dissolution, and diagenesis at the sea floor. *The Dynamic Environment of the Ocean Floor*, eds Fanning, KA, Manheim, FT (Lexington Books), pp. 115-145.

25   Rickard, D, Sjöberg, L (1983) Mixed kinetic control of calcite dissolution rates. *Amer. J. Sci.* 283, 815-830.

26   Boudreau BP, Jørgensen BB (2001) The Benthic Boundary Layer (Oxford).

27   Boudreau BP, Middelburg JJ, Meysman FJR (2010) Carbonate compensation dynamics. *Geophys Res Lett* 37.

28   Archer D, Emerson S, Reimers C (1989) Dissolution of calcite in deep-sea sediments: pH and O_2 microelectrode results. *Geochim. Cosmochim. Acta* 53: 2831–2845.

29   Archer D (1991) Modeling the calcite lysocline. *J. Geophys. Res.* 96: 17037-17050.

30   Berelson WM, Hammond DE, Cuttert GA (1991) *In situ* measurements of calcium carbonate dissolution rates in deep-sea sediments. *Geochim. Cosmochim. Acta* 54: 3013-3010.

31   Berelson, WM, Hammond, DE, McManus J, Kilgore TE (1994) Dissolution kinetics of calcium carbonate in equitorial Pacific sediments. *Global Biogeochem. Cycles* 8: 219-235.

32   Jahnke RA, Craven DB, Gaillard JF (1994) The influence of organic matter diagenesis on $CaCO_3$ dissolution at the deep-sea floor. *Geochim. Cosmochim. Acta* 58: 2799–2809, doi:10.1016/0016-037(94)90115-5.

33   Martin, WR, Sayles FL (1996) CaCO*3* dissolution in sediments of the Ceara Rise, western equitorial Atlantic. *Geochim. Cosmochim. Acta* 60: 243-263.

34   Jahnke RA, Craven DB, McCorkle DC, Reimers CE (1997) $CaCO_3$ dissolution in California continental margin sediments: the influence of organic matter remineralization. *Geochim. Cosmochim. Acta* 61: 3587-3604.

35   Hales B, Emerson S (1997) Evidence in support of first-order dissolution kinetics of calcite in seawater. *Earth Planet. Sci. Lett.* 148: 317– 327, doi:10.1016/S0012-821X(97)00017-4.

36   Zeebe RE (2007) Modeling CO_2 chemistry, $\delta^{13}C$, and oxidation of organic carbon and methane in sediment porewater: implications for paleo-proxies in benthic foraminifera. *Geochim. Cosmochim. Acta* 71: 3238-3256.

37   Broecker WS, Peng TH (1982) *Tracers in the Sea* (Lamont-Doherty Geological Observatory, Columbia University, Palisades, New York, 1982), pp. 705.

38   Morse JW (1978) Dissolution kinetics of calcium carbonate in sea water: VI. The near-equilibrium dissolution kinetics of calcium carbonate-rich deep sea sediments: *American Journal of Science*, v. 278, no. 3, p. 344-353.

39   Keir RS (1980) The dissolution kinetics of biogenic calcium carbonates in seawater: *Geochimica et Cosmochimica Act*a, v. 44, no. 2, p. 241-252.

40   Walter LM, Morse JW (1985) The dissolution kinetics of shallow marine carbonates in seawater: A laboratory study: *Geochimica et Cosmochimica Acta*, v. 49, no. 7, p. 1503-1513.

41   Subhas AV, et al. (2015) A novel determination of calcite dissolution kinetics in seawater: *Geochimica et Cosmochimica Acta*, v. 170, p. 51-68.

42   Glud RN, Gundersen JK, Revsbech NP, Jørgensen BB (1994) Effects on the benthic diffusive boundary layer imposed by microelectrodes: *Limnology and Oceanography*, v. 39, no. 2, p. 462-467.

43   Broecker WS, Klas M, Clark E (1991) The Influence of $CaCO_3$ Dissolution on Core Top Radiocarbon Ages for Deep-Sea Sediments: *Paleoceanography*, v. 6, no. 5, p. 593-608.

44   Keir RS, Michel RL (1993) Interface dissolution control of the ^{14}C profile in marine sediment: *Geochimica et Cosmochimica Acta*, v. 57, no. 15, p. 3563-3573.

45   Oxburgh R (1998) The Holocene preservation history of equatorial Pacific sediments: *Paleoceanography*, v. 13, no. 1, p. 50-62.